Dry sliding wear behaviour of cold-sprayed Cu-MoS_2 and Cu-MoS_2-WC composite coatings: the influence of WC

Yinyin Zhang[1], Yakov Epshteyn[2], and Richard R. Chromik[1]*

[1]Department of Mining and Materials Engineering, McGill University, 3610 University Street, Montreal, QC, H3A 0C5, Canada

[2]Climax Molybdenum Company, 333 North Central Ave., Phoenix, AZ 85004, United States

*: corresponding author: richard.chromik@mcgill.ca (Richard R. Chromik)

Abstract

Cold-sprayed Cu-MoS_2 and Cu-MoS_2-WC composite coatings were studied for their sliding wear performance in dry nitrogen. Presence of WC particles reduced friction coefficient and improved wear resistance. Dynamics of material transfer, chemical and phase composition of third bodies in the contact were examined. WC particles helped to form transfer films and smooth wear tracks; while rough wear tracks with evidence of detachment were observed for the Cu-MoS_2. Subsurface microstructure of the wear tracks showed major microstructural change occurred around WC particles. Microstructure and thickness of the tribolayers at 100 and 1000 cycles exhibited minor changes. However, for Cu-MoS_2, microstructural change took place more extensively with sliding, leading to unstable tribolayers, which contributed to crack formation, detachment, and eventually high wear.

Key words: dry sliding wear; cold-sprayed Cu-MoS_2-WC; third body behaviour; subsurface microstructure.

1 Introduction

Self-lubricating metal matrix composites (SLMMCs) have been used as dry bearing materials due to their improved tribological performance [1]. There is a long history of research on these materials with one of the first reports by Bowden, who studied incorporation of MoS_2 in Cu and Mo and found that the composites showed low friction coefficients of around 0.13 and 0.06, respectively [2]. Many other metals such as silver, iron, nickel have been used as metal matrices with MoS_2 fillers to achieve low friction ranging from 0.04 to 0.26 [1]. SLMMCs often exhibit a best combination of friction and wear behaviour at an optimum (or 'critical') lubricant content. When the lubricant content is optimized, researchers typically find that stable lubricating films are formed without too much debit in the mechanical properties of the composite, which will increase with lubricant content [3, 4]. Wu et al. [3] investigated hot-pressed Ni/MoS_2 composites with various MoS_2 content. They found the optimum MoS_2 content was 60 wt.%, which generated the lowest friction of around 0.1 and the lowest wear rate of 10^{-4} to 10^{-5} mm^3/Nm. Dhanasekaran et al. [5] found that for sintered steel/MoS_2 composites, addition of 3% MoS_2 yielded lower friction and wear than that of 5% MoS_2, which caused declined hardness and strength. Incorporation of ceramics into metal-solid lubricant composite making hybrid composites is a common strategy to improve strength and wear resistance of SLMMCs [6-11]. Narayanasamy et al. [8] showed improved mechanical property and wear resistance when adding TiC to Mg/MoS_2 composites using powder metallurgy. The composite with 10 wt.% TiC and 5 wt.% MoS_2 exhibited the utmost improvement in tribological performance.

For SLMMCs, conventional manufacturing processes such as casting, laser cladding, powder metallurgy, and thermal spray, will introduce high temperature that can cause decomposition and phase transformation of the solid lubricants. Brittle compound $CuMo_2S_3$ were found in sintered Cu-MoS_2 composites, and it causes MoS_2 to be ineffective as a solid lubricant, resulting in high friction [12]. These issues can be overcome by using a less energetic process, such as cold spray. This relatively new coating process, uses a de Laval nozzle and a high pressure gas to accelerate powders to supersonic velocities (500-1200 m/s). Powders deposit onto a substrate in the solid state [13-15]. During cold spraying, since the gas is preheated to temperatures that are below melting temperature of feedstock, melting and decomposition that are commonly observed in the traditional manufacturing process can be minimized or eliminated [13-15].

In the present study, Cu-MoS_2 and Cu-MoS_2-WC composite coatings were deposited using cold spray. Their sliding wear performance in dry nitrogen was investigated, with the focus on the influence of WC particles on friction, wear, third body behaviour, as well as tribologically-modified microstructure evolution.

2 Experimental methods

2.1 Coating deposition and characterization

A commercially available cold spray system (PCS800, Plasma Giken, Japan) equipped with two powder feeders was used for coating deposition. Dual feeding technique permits carrying powders separately to the gun and the fractions of each component are monitored by adjusting their feed rates. In the present work, spherical Cu powder (Tekna Advanced Materials Inc., d_{50} = 26 µm), spherical MoS_2 powder (Climax, d_{50} = 68 µm), and spherical WC powder (Tekna Advanced Materials Inc., d_{50} = 30 µm) were used as feedstocks (see Fig. 1). The Cu-MoS_2 composite was fabricated by feeding Cu and MoS_2 from different hoppers with feeding rates of 34.8 and 3.6 g/min, respectively, which achieved a mass fraction of MoS_2 around 9% in the feedstock. For Cu-MoS_2-WC coating, in one hopper was a mix of Cu and WC (Cu + 19 wt.% WC), prepared by mechanical mixing, in the other hopper was pure MoS_2 powder. They were fed at average rates of 39.4 and 3.6 g/min, respectively, achieving a mass fraction of MoS_2 around 8% in the feedstock. Compressed nitrogen with gas pressure and temperature of 5 MPa and 800 °C, respectively was the carrying gas. Aluminium alloy AA6061 was used as substrates. They were cleaned using acetone, sand-blasted, and then preheated to around 170 °C by traversing the spray gun over the substrate slowly (5 mm/s) with the heated processing gas only. During coating deposition, the gun traverse speed was 60 mm/s. Those spraying parameters were also applied in our previous work for fabrication of Cu-MoS_2 composite [16, 17].

The coatings were then cross sectioned, cold mounted, mechanically ground and polished to 0.05 µm colloidal silica. At least ten SEM micrographs, specifically backscattering electron (BSE) images with a magnification of 1000×, were taken and used to measure MoS_2 and WC concentration by image analysis through pixel count. Microhardess testing (Clark microhardness tester, AM-100AT) was carried out using a normal load of 200 gf and a dwell time of 15 s. It’s

worth to note that for the Cu-MoS_2-WC composite coating, indentation was performed on the matrix, i.e. Cu-MoS_2 only.

2.2 Sliding wear tests in dry nitrogen

Top surface of the Cu-MoS_2 and Cu-MoS_2-WC composite coatings were ground and polished following the above procedure. Sliding wear tests were then conducted on the polished surfaces using a custom-built reciprocating tribometer [18, 19]. Friction force was measured via a piezoelectric sensor at a sampling rate of 800 Hz. The counterfaces were polycrystalline alumina spheres with a diameter of 6.35 mm, which are a common counterface material for tribological testing of metal matrix composites [20, 21] and is a material commonly used for cutting tools, guides and extrusion dies [22]. A normal force of 5 N was applied to the alumina sphere. The sliding speed was 2 mm/s and the wear track length was 4 mm. The only variable during the test was the cycle number, which was set at 100 cycles and 1000 cycles. Three repeats at each condition were carried out. All the tests were conducted in dry nitrogen (oxygen content was below 0.5 %) and room temperature (21-24°C). Sliding tests in dry nitrogen are often used for MoS_2 containing materials as they exhibit better tribological performance in vacuum and inert gases than in humid air [23].

2.3 Post-test characterization of wear tracks and counterfaces

To examine wear track topography and measure wear rate, the wear tracks were scanned by a Wyko NT8000 non-contact optical interferometer. Cross-sectional profiles of the wear tracks were extracted, data points below the unworn surface were integrated to calculate the net volume of worn material.

To examine the third body behaviour in the contact, morphology of the wear tracks and counterfaces was examined by a cold field emission scanning electron microscope (SEM) (FEI, Inspect F50, USA) and a light optical microscope, MoS_2 distribution at the wear tracks and counterfaces was examined by either a SEM (Hitachi, SU-8230, Japan) equipped with an annular EDX detector or an inVia Raman microscope (Renishaw, UK) mounted with an Ar^+ ion ($\lambda = 514.5$ nm) laser source.

Cross-sectional microstructure of the wear tracks was observed using a focused ion beam/scanning electron microscope (FIB/SEM) (FEI, Helios NanoLab DualBeam, USA). The FIB cuts were performed perpendicular to the sliding direction. Electron channeling contrast images (ECCI) were taken using a BSE detector to examine subsurface microstructure. This technique permits observation of defects such as grain boundary, deformation bands, etc. inside polycrystalline materials [24]. The theory of ECCI technique has been developed over forty years and has been elaborated elsewhere [25, 26].

3 Results

3.1 Cold-sprayed coatings

Cross sectional micrographs of Cu-MoS_2 and Cu-MoS_2-WC composite coatings are shown in Fig. 2a and b, respectively. The dark contrast along the particle boundaries is MoS_2, as shown in our previous work [16, 17]. In Fig.2b, WC particles are distributed homogeneously throughout the coating. Top view morphology of the Cu-MoS_2-WC composite coating and corresponding EDX map of sulphur (see Fig. 2c and 2d) suggest MoS_2 was deposited along particle boundaries. The average MoS_2 and WC contents measured based on BSE images are: 3.22 ± 1.40 vol.% MoS_2 in the Cu-MoS_2, 4.03 ± 1.23 vol.% MoS_2 and 7.5 ± 2.19 vol.% WC in the Cu-MoS_2-WC composite coating. The deposition efficiencies of Cu-MoS_2 and Cu-MoS_2-WC are 51% and 56%, respectively.

As seen in Fig. 3, average microhardness of the Cu-MoS_2 and Cu-MoS_2-WC are much lower than the pure Cu, which indicates incorporation of MoS_2 by cold spray degraded hardness. The Cu-MoS_2 and Cu-MoS_2-WC have similar average hardness to one another, so do the variations of hardness, yet larger than that of pure Cu.

3.2 Friction and wear

Average coefficients of friction of Cu-MoS_2, Cu-MoS_2-WC, and pure Cu throughout the test to 1000 cycles are plotted in Fig. 4. They show similar friction behavior i.e. a running-in peak within the first 100-200 cycles, followed by a steady state value. However, composite coatings show lower friction coefficients. For Cu-MoS_2, during the short running-in of less than 100 cycles,

friction increases up to a peak value of roughly 0.4 and decreases quickly to 0.38-0.39, and then stays constant. While for Cu-MoS_2-WC, during running-in, the friction increases to a peak value of around 0.33, then decreases gradually until around 200 cycles, when the steady-state vale of 0.27-0.28 is reached.

Triboimage, as shown in Fig. 5, plots friction along the wear track length (Y axis) with cycle numbers (X axis) via a color legend. For Cu-MoS_2 (see Fig. 5a), lower friction stripes observed in the triboimage, which indicates lack of uniformity of friction distribution in the wear track. In contrast, Cu-MoS_2-WC (see Fig. 5b) exhibits a greater uniformity in friction throughout the wear track after the first 50-100 cycles.

Wear track topography (see Fig. 6) of Cu-MoS_2 and Cu-MoS_2-WC reveals differences in wear behaviour. The Cu-MoS_2 wear track had uneven depth at 100 cycles (see Fig. 6a), with some areas (showing as dark) as deep as 4-5 µm, while the others were slightly deeper than 1 µm. At 1000 cycles (see Fig. 6b), this feature remained, showing as dark patches with the depth ranging between 4 and 5 µm, while the other areas were roughly 2 µm in depth. The variation in wear track depth was shown as a high deviation on depth measurement, as seen in Fig. 7a. However, the Cu-MoS_2-WC wear tracks were relatively more uniform and shallower (see Fig. 6c and d). At 100 cycles, it was mostly 1-1.5 µm deep and a few shallower areas e.g. 0.5-1 µm. The uniformity was observed at 1000 cycles, as shown in Fig. 6d, yet the depth varied within a slightly wider range, i.e. between 1-2 µm.

Wear rates of Cu-MoS_2 and Cu-MoS_2-WC at 100 and 1000 cycles are shown in Fig. 7b. Both coatings wore faster during the first 100 cycles, around 210×10^{-6} mm^3/Nm for Cu-MoS_2, while 123×10^{-6} mm^3/Nm for Cu-MoS_2-WC. The wear rate became lower at 1000 cycles, with 35×10^{-6} mm^3/Nm for Cu-MoS_2 and 19×10^{-6} mm^3/Nm for Cu-MoS_2-WC. Cu-MoS_2-WC exhibited lower wear rates during the whole sliding testing.

3.3 Morphology and phase composition of the Cu-MoS_2 third bodies

Fig. 8 shows morphology of the Cu-MoS_2 wear track after 1000 cycles. It is mostly smooth, yet includes several detachments of material (see Fig. 8a and b). The dimension of the detachments can be as large as around 100 µm. A closer view of the detachment exhibits layered feature of

tribolayer, that suggests Cu experienced extensive plastic deformation, by which the velocity difference between the two rubbing surfaces were accommodated [27]. Scoring grooves were visible across the detached area, indicative of microplowing. In addition, cracks were frequently found close to the location where detachment occurred (see Fig. 8c). They are long, wavy, and tend to be perpendicular to the sliding direction.

Phase composition in the wear tracks examined by Raman spectroscopy exhibits MoS_2 distribution evolution with sliding (see Fig. 9). At 100 cycles, the dark contrast under optical microscope was patchy and smeared along the sliding direction (see Fig. 9a). The first spot tested was on the gray material, as indicated in Fig. 9a, and it was identified as MoS_2 according to the two typical peaks around 400 cm^{-1} (see Fig. 9b). The peaks below 300 cm^{-1} and above 600 cm^{-1} Raman shift were identified as Cu_2O [28]. Following the trail of MoS_2 smearing, spot 2 only exhibited weak peaks of MoS_2. As all the measurements were taken at the same condition, MoS_2 content can be qualitatively indicated by the peak intensity, therefore spot 2 had lower MoS_2 content than spot 1. At 1000 cycles, material close to a detachment was examined. Similarly, a piece of gray material, marked as 1 in Fig. 9c, was identified as a mix of MoS_2 and Cu_2O. Only weak MoS_2 peaks were found at spots 2 and 3, yet no presence of MoS_2 or other Raman active material was detected at spot 4 (see Fig. 9c and d). The above observation of MoS_2 distribution suggests MoS_2 was smearing out at the beginning of the sliding, yet constrained within a small area of less than 20 μm along the sliding direction. Such behavior contributed to formation of MoS_2 patches in the wear track, resulting in partial lubricating, which was the main difference from MoS_2 blanket fabricated by PVD and CVD [29-32].

Micrographs of the counterfaces at 100 and 1000 cycles (see Fig. 10a and b) show fine coppery debris adhering to the contact area. They are mostly a few microns in size. Raman spectra obtained from all the wear debris show only few of them contained MoS_2 (see Fig. 10c). This suggests copper-alumina contact was the main contact interface during sliding. In addition, at 100 cycles, a large ejected wear debris was deposited outside the contact. At 1000 cycles, the counterface was scratched on one side, which could be caused by a piece of work hardened Cu.

3.4 Morphology and phase composition of the Cu-MoS_2-WC third bodies

Comparing to the Cu-MoS_2 wear track at 1000 cycles, Cu-MoS_2-WC wear track does not have large-scale detachments (see Fig. 11a). Only few with a length scale of about 10 µm was introduced, as shown in Fig. 11b and c. Their edges appeared as tongue-shaped morphology, an evidence of material smearing and plastic deformation [33]. The WC particles are embedded in the wear track (see Fig. 11a and b), and covered fully or partly with a thin layer of the matrix material. Therefore the WC particles were sitting just underneath the topmost surface of the wear track during sliding, leading to a scenario of a hard material with a soft "skin". Its impact on friction is interpreted in details in the discussion section.

Sliding-induced MoS_2 redistribution in the wear tracks was examined by high resolution EDX maps of sulfur (S) or molybdenum (Mo), indicative of MoS_2, as shown in Fig. 12. At 100 cycles (see Fig. 12a, b and c), MoS_2 had smeared out from the original location, i.e. particle boundaries (see Fig. 2d), showing as MoS_2-containg patches. Dimension of the patches largely depends on local MoS_2 content. At 1000 cycles, MoS_2 patches are remaining on the wear track (see Fig. 12c and d), which suggests MoS_2 is replenished as wear continues. The spread of MoS_2 in Cu-MoS_2-WC during sliding is similar to that in Cu-MoS_2 examined by Raman spectroscopy.

Micrographs of the counterfaces show coppery debris that adhere to the contact area (see Fig. 13a and b). Dimension of the debris is comparable to that of Cu-MoS_2 (see Fig. 10a and b). However, much more debris is attached at the 1000-cycle counterface. MoS_2 was detected in some of those wear debris on both 100- and 1000- cycle counterfaces (see Fig. 13c).

3.5 Subsurface microstructure of the Cu-MoS_2 wear tracks

As seen in Fig. 14a, a FIB cut was performed across a detachment at the 100-cycle wear track. It exhibited mild modification in microstructure after such a short duration of sliding. Fig. 14c shows an area where the top layer has been detached, therefore initial as-sprayed microstructure is observed, as evidenced by defect contrast of deformation bands, which has been commonly found in cold sprayed Cu [24]. However, for the area where the material was not removed (see Fig. 14 a and d), on the top of the wear track is a thin layer, less than 500 nm thick, of ultrafine grains (UFG), below that is one to two grain layer of coarse grains (CG). The overall thickness of the sliding modified microstructure at 100 cycles is less than 1 µm.

At 1000 cycles, two FIB cuts were carried out in the wear track, with cut 1 at a cracked area (see Fig. 15a and b), a typical feature showed in Fig. 8c, while cut 2 at a smooth area (see Fig. 15c and d). Their locations were indicated in Fig. 8a. In Fig. 15b, the sliding-modified layer is 3.5-5.5 μm thick. It is featured as a mix of UFGs, coarse equiaxed grains, and small elongated grains. Cracks are commonly observed in the tribolayer, some of them are filled with MoS_2. However, subsurface microstructure of the smooth area shows continuous feature without any cracks (see Fig. 15c and d). Vortices of the UFGs become more pronounced than that at 100 cycles. Between the vortices are large equiaxed grains, and beneath those microstructures are small elongated grains. Fig. 15d is a closer view of the area where grain boundaries are not well defined, as indicated by the white arrows. The penetration depth of the UFGs was 2-5 μm, while the overall sliding-induced microstructure is as deep as around 12 μm, which is much deeper than that in the cracked area.

3.6 Subsurface microstructure of the Cu-MoS_2-WC wear tracks

The subsurface microstructure of Cu-MoS_2-WC wear tracks appear different features due to the presence of WC particles. Fig. 16a-c show microstructure at a WC particle after 100 cycles. UFGs are exclusively aside the WC particle, with around 400 nm deep on one side, 1.8 μm deep on the other side. MoS_2 has been mixed with the UFGs, which was examined by the EDX map in Fig. 16c. Beneath the UFGs are CGs that are mostly equiaxed and penetrate to the first body around 4 μm deep. Both UFGs and the entire sliding-modified microstructure are deeper than that of the 100-cycle Cu-MoS_2 wear track. Microstructure far from the WC particle is shown in Fig. 16d. Vortices of fine grains are on the top, followed by a layer of CGs. It is worth to note that grain size of the top fine grains (FG) in the vortices is larger than the UFGs yet smaller than the CGs. The thickness of the sliding modified structure is 1.5-4 μm.

At 1000 cycles, the sliding-induced microstructure exhibits similar features to that at 100 cycles. Fig. 17a-c show microstructure around a WC particle, while Fig. 17d is far from the WC particles. UFGs are only generated aside the WC particle and their maximum depths are around 1.5 μm on the left side, 3.0 μm on the right side (see Fig. 17b and c), same length scale to that at the 100 cycles. Vortices of FGs are on the top that is far away from the WC particle. Both UFGs and FGs are surrounded by a layer of CGs and smaller grains. Interfaces between the sliding-modified and the as-sprayed material indicate microstructural change occurs preferably around the WC particle

and the thickness is 3-5 µm. Microstructure far from the WC particles is shown in Fig. 17d, in which vortices of FGs are on the top, followed by a layer of CGs. A lamellar structure is also found beneath the CGs. Cracks are visible between the layers that contain mostly elongated grains. Comparing to the layered structure in Cu-MoS_2 (see Fig. 15b), this structure is more compacted.

4 Discussion

Self-lubricating copper matrix composites Cu-MoS_2 and Cu-MoS_2-WC coatings were fabricated by cold spray. Adding 10 vol.% WC particles to the feedstock did not modify significantly the deposition in terms of deposition efficiency, MoS_2 retention, as well as hardness of the composite. Even though the slightly higher hardness of Cu-MoS_2-WC probably due to the impact of hard phases, the "hammering effect" of hard phases was not as pronounced as that observed by some other researchers [33, 34]. This might be because the hard phase fraction was not high enough comparing to that in the literature, i.e. more than 30 vol.% [34]. Another possibility could be that microhardness testing was influenced more by the MoS_2-induced hardness loss such that the "hammering effect" of WC particles was masked. The large standard deviation of microhardness values of Cu-MoS_2 and Cu-MoS_2-WC was caused by locally poor uniformity of MoS_2 throughout the coatings. Incorporation of 7.5 ± 2.19 vol.% WC particles into coating did not improve dramatically inhomogeneous MoS_2 distribution.

When those composite coatings were subjected to sliding wear tests, the distinct friction behaviour of Cu-MoS_2 and Cu-MoS_2-WC suggests WC was not only helpful on reduction of average friction but also on homogenization of friction throughout the wear track (see Fig. 4 and 5, respectively). The friction reduction due to reinforced particles can be well interpreted using classical theory developed by Bowden and Tabor [18, 35], where friction force (F) is product of real contact area (A) and shear strength of lubricant material (τ), friction coefficient can be expressed as:

$$\mu = \frac{F}{L} = \frac{A \cdot \tau}{L} = \frac{\tau}{P_H} = \frac{\tau_0}{P_H} + \alpha \qquad \text{(eq. 1)}$$

where τ_0 is the interfacial shear strength, and α is the lowest attainable friction coefficient for a given friction couple. In principle, a hard material tends to reduce contact area and ought to provide a low friction coefficient. This was confirmed by the top view morphology of Cu-MoS_2-WC wear track (see Fig. 8), where WC particles were embedded in the wear track with a thin layer of Cu or

Cu/MoS_2 smeared on the top, leading to a scenario of a hard material with a soft "skin". Influence of hard particles on friction coefficient has two folds. One is to reduce friction, in which the hard particles are embedded in the wear track, offering a hardened tribolayer and decreasing contact area. However, if the hard particles remain at the contact and serve as abrasives, the friction coefficient tends to increase [36]. Which mechanism dominates largely depends on running condition. Zhan et al. [36] found the former plays a major role under a lower normal load, while the latter under a high normal load.

For wear behaviour, the presence of WC particles reduced wear rate and produced a homogeneous wear track in terms of depth. Even though the homogeneously distributed WC particles did not improve bonding strength between Cu and MoS_2 (similar standard deviations of hardness values in Fig. 3), they increased the load bearing capacity and prevented penetration of large plastic deformation with sliding continuously, and therefore improved wear resistance. Such role of hard phases in MMCs has been well established. Deshpande et al. [37] observed a considerable decrease in wear rates in Cu-WC composites when sliding against sintered SiC abrasive disk, and the wear resistance was more significantly improved at higher normal loads. Shockley et al. [38] found similar results in cold sprayed Al-Al_2O_3 composites sliding against sapphire, in which the wear rates and their standard deviation were around one order magnitude lower than the pure Al counterpart.

Material transfer at the contact and microstructure of the third bodies were examined to better understand the friction and wear behaviour. For both composite coatings, redistribution of MoS_2 followed the same manner. It was smeared out from the particle boundaries once sliding commenced and formed MoS_2 patches. They were replenished as sliding continued (see Fig. 9 and 12). However, much more wear debris containing MoS_2 stuck on the counterface for the Cu-MoS_2-WC composite coating, while almost all wear debris was removed during sliding for the Cu-MoS_2 composite coating at 1000 cycles (see Fig. 10 and 13). More MoS_2-containing wear debris could generate discontinuous MoS_2 transfer film that separated the initial contact, and therefore achieve low friction. The rapid removal of wear debris suggested more active material transfer at the contact of Cu-MoS_2 coating. Furthermore, cracks and large detachments occurred at the Cu-MoS_2 wear tracks (see Fig. 8), while none of these features was observed in the Cu-MoS_2-WC wear track (see Fig. 11). Cross section of the lamella structure showed that there were more highly compacted

layers in the Cu-MoS_2-WC wear track than that in the Cu-MoS_2 wear track (see Fig. 15b and 17d). This again indicated more active material transfer at the Cu-MoS_2 contact, leading to higher wear rate. In addition, formation of the cracks (see Fig. 8) was interpreted by Berthier et al. [27, 39, 40]. They were formed because of high skin shear stress such that displacements can be accommodated more flexibly than an entire piece of material. This can be confirmed by subsurface microstructure observation, where the cracked area showed shallower sliding-modified microstructural change comparing to the smooth area (see Fig. 15).

Subsurface microstructure of the wear tracks showed more information on the role of WC particles during sliding. In Cu-MoS_2-WC wear tracks, UFGs were only formed aside the WC particles (see Fig. 16 and 17), while for Cu-MoS_2, UFGs were commonly found on the top of the wear track. This suggests WC was load bearing and shielded the other parts from severe plastic deformation and eventually material transfer. Even though the thickness of UFGs was higher than that in the Cu-MoS_2-WC wear track after 100 cycles, it kept constant even after 1000 cycles, which was shallower than Cu-MoS_2 UFGs after 1000 cycles (see Fig. 15b and 15c). That indicates microstructural change was minor from 100 to 1000 cycles, and hence a more stable tribolayer was formed in the Cu-MoS_2-WC sliding system. As UFGs were work hardened, it was more readily for crack nucleation and propagation. This is probably the reason why cracks and large detachments were more frequently observed in the Cu-MoS_2 wear tracks (see Fig. 8). In addition, as it was probably impossible for the WC particles to be plastically deformed during sliding, they can be acting as “extremely hard grain orientation” for bulging and fold formation, which were identified as precursors of wear debris. This model was developed by Beckmann et al. [41] using large-scale molecular dynamics (MD) simulations, where they showed on polycrystalline metal surfaces, sliding preferentially activated suitably oriented grains i.e. soft grains rather than hard grains to form protrusions and bulges. Therefore, engineering approaches that minimize soft grains and/or introduce hard grains could significantly reduce bulging and fold formation which eventually improve wear resistance [41].

What’s more, vorticity microstructure was formed only after a short duration of sliding i.e. 100 cycles in both composite coatings (see Fig. 14-17). This material flow pattern was believed to be similar to that occurred in fluid flow [42]. Luo et al. [43] studied microstructural evolution sequence under sliding and found those waviness and vortices were formed at the beginning of

sliding and it was initiated by gradients of strain and strain rate during sliding. Another pronounced feature of the sliding-induced microstructure is complexity of the lamella structure in the Cu-MoS_2 composite that includes UFGs, CGs, as well as elongated grains (see Fig. 15b). That was probably because third bodies had undergone different levels of deformation, i.e. the coarse grains did not experienced severe plastic deformation while formation of the UFG was the result of accumulation of severe plastic deformation. Similar third body microstructure was also observed in pure Cu rubbing against steel [44], and Al sliding against Al_2O_3 [38].

5 Conclusions

A Cu-MoS_2-WC composite coating was fabricated by cold spray and it exhibited comparable MoS_2 content and microhardness with that of Cu-MoS_2 coating. However, sliding wear experiments conducted in dry nitrogen showed that friction of Cu-MoS_2-WC against alumina was lower and more uniform throughout the wear track, as well as lower and more homogeneous wear rates. Material transfer in the contact and microstructure of third bodies suggest that was due to the presence of WC particles.

Wear track morphology showed a large scale of detachment occurred in Cu-MoS_2 wear tracks, while smooth Cu-MoS_2-WC wear tracks with only small detachments. The WC particles were sitting just underneath the wear track and provided a scenario of a hard material with soft “skin”, which obtained lower friction. MoS_2 redistribution exhibited similar manner on the wear tracks for both coatings, yet more MoS_2-containing debris attached to the Cu-MoS_2-WC counterface after 1000 cycles, probably forming a transfer film that separate the initial sliding contact, and therefore reduced the friction.

Subsurface microstructure of the wear tracks revealed contrast between those two coatings and influence of the WC particles. Major microstructural change only occurred around WC particles and minor changes were observed after a longer sliding, which suggests WC particles were load bearing and helped to form a more stable tribolayer; while for Cu-MoS_2, server plastic deformation and microstructural refinement occurred more extensively, leading to a thick, unstable tribolayer. This produced a more active material transfer in the contact and contribute to cracking, detachment, and eventually high wear.

Acknowledgements

The authors gratefully acknowledge the financial support from Natural Sciences and Engineering Research Council (NSERC) of Canada. They gratefully acknowledge technical support on scanning electron microscopy from Mr. Nicolas Brodusch and Dr. Hendrix Demers, and on FIB cut from Ms. Line Mongeon. The authors acknowledge Tekna Plasma Systems Inc. for donation of the powder and administrative support from Drs. Phuong Vo, Eric Irissou and Jean-Gabriel Legoux (the NRC) and Stephen Yue (McGill University) and technical support from Mr. Jean Francois Alarie at the McGill Aerospace Materials and Alloy Design Center (MAMADC) cold spray facility.

References

1. Lansdown, A.R., *Chapter 12 Composites*, in *Tribology Series*, A.R. Lansdown, Editor. 1999, Elsevier. p. 207-244.
2. Bowden, F. and K. Shooter, *Frictional Behaviour of Plastics Impregnated with Molybdenum Disulphide, Res. Appl.* Ind, 1950. **3**: p. 384.
3. Wu, Y., F. Wang, Y. Cheng, and N. Chen, *A study of the optimization mechanism of solid lubricant concentration in NiMoS2 self-lubricating composite.* Wear, 1997. **205**(1): p. 64-70.
4. Zhang, Y. and R.R. Chromik, *Tribology of Self-Lubricating Metal Matrix Composites*, in *Self-Lubricating Composites*. 2017, Springer.
5. Dhanasekaran, S. and R. Gnanamoorthy, *Dry sliding friction and wear characteristics of Fe–C–Cu alloy containing molybdenum di sulphide.* Materials & design, 2007. **28**(4): p. 1135-1141.
6. Miracle, D.B., *Metal matrix composites – From science to technological significance.* Composites Science and Technology, 2005. **65**(15–16): p. 2526-2540.
7. Suresha, S. and B.K. Sridhara, *Wear characteristics of hybrid aluminium matrix composites reinforced with graphite and silicon carbide particulates.* Composites Science and Technology, 2010. **70**(11): p. 1652-1659.
8. Narayanasamy, P., N. Selvakumar, and P. Balasundar, *Effect of Hybridizing MoS2 on the Tribological Behaviour of Mg–TiC Composites.* Transactions of the Indian Institute of Metals, 2015. **68**(5): p. 911-925.
9. Xu, J., W. Liu, and M. Zhong, *Microstructure and dry sliding wear behavior of MoS2/TiC/Ni composite coatings prepared by laser cladding.* Surface and Coatings Technology, 2006. **200**(14–15): p. 4227-4232.
10. Rajkumar, K. and S. Aravindan, *Tribological performance of microwave sintered copper–TiC–graphite hybrid composites.* Tribology International, 2011. **44**(4): p. 347-358.
11. Suresha, S. and B.K. Sridhara, *Effect of addition of graphite particulates on the wear behaviour in aluminium–silicon carbide–graphite composites.* Materials & Design, 2010. **31**(4): p. 1804-1812.

12. Kato, H., M. Takama, Y. Iwai, K. Washida, and Y. Sasaki, *Wear and mechanical properties of sintered copper–tin composites containing graphite or molybdenum disulfide.* Wear, 2003. **255**(1): p. 573-578.
13. Assadi, H., F. Gärtner, T. Stoltenhoff, and H. Kreye, *Bonding mechanism in cold gas spraying.* Acta Materialia, 2003. **51**(15): p. 4379-4394.
14. Irissou, E., J.-G. Legoux, A. Ryabinin, B. Jodoin, and C. Moreau, *Review on cold spray process and technology: Part I-Intellectual property.* Journal of Thermal Spray Technology, 2008. **17**(4): p. 495-516.
15. Champagne, V.K., *The cold spray materials deposition process: fundamentals and applications*. 2007: Elsevier.
16. Zhang, Y., J.M. Shockley, P. Vo, and R.R. Chromik, *Tribological Behavior of a Cold-Sprayed Cu–MoS2 Composite Coating During Dry Sliding Wear.* Tribology Letters, 2016. **62**(1): p. 1-12.
17. Zhang, Y., S. Descartes, P. Vo, and R.R. Chromik, *Cold-Sprayed Cu-MoS2 and Its Fretting Wear Behavior.* Journal of Thermal Spray Technology, 2016. **25**(3): p. 473-482.
18. Chromik, R., H. Strauss, and T. Scharf, *Materials phenomena revealed by in situ tribometry.* JOM, 2012. **64**(1): p. 35-43.
19. Strauss, H.W., R.R. Chromik, S. Hassani, and J.E. Klemberg-Sapieha, *In situ tribology of nanocomposite Ti–Si–C–H coatings prepared by PE-CVD.* Wear, 2011. **272**(1): p. 133-148.
20. Blau, P.J., *Appendix: Static and Kinetic Friction Coefficients for Selected Materials*, in *ASM Handbook: Vol. 18. Friction, Lubrication, and Wear Technology*, P.J. Blau, Editor. 1992, ASM International. p. 101-111.
21. Li, J.L. and D.S. Xiong, *Tribological properties of nickel-based self-lubricating composite at elevated temperature and counterface material selection.* Wear, 2008. **265**(3): p. 533-539.
22. Glaeser, W.A., *Introduction to Materials for Friction and Wear Applications*, in *ASM Handbook: Vol. 18. Friction, Lubrication, and Wear Technology*, P.J. Blau, Editor. 1992, ASM International. p. 812–815.
23. Scharf, T.W. and S.V. Prasad, *Solid lubricants: a review.* Journal of Materials Science, 2012. **48**(2): p. 511-531.
24. Zhang, Y., N. Brodusch, S. Descartes, R.R. Chromik, and R. Gauvin, *Microstructure Refinement of Cold-Sprayed Copper Investigated By Electron Channeling Contrast Imaging.* Microscopy and Microanalysis, 2014. **20**(05): p. 1499-1506.
25. Howie, A., *Theory of diffraction contrast effects in the scanning electron microscope.* Quantitative Scanning Electron Microscopy, Holt DB, Muir M., Grant P. & Boswarva I.(Eds.), 1974: p. 183-212.
26. Joy, D.C., D.E. Newbury, and D.L. Davidson, *Electron channeling patterns in the scanning electron microscope.* Journal of Applied Physics, 1982. **53**(8): p. R81-R122.
27. Berthier, Y., *Experimental evidence for friction and wear modelling.* Wear, 1990. **139**(1): p. 77-92.
28. Hesse, J. and A. Compaan, *Resonance Raman studies of annealing in He ⁻, Na ⁻, Cd ⁻ implanted cuprous oxide.* Journal of Applied Physics, 1979. **50**(1): p. 206-213.
29. Lince, J.R., *Tribology of co-sputtered nanocomposite Au/MoS2 solid lubricant films over a wide contact stress range.* Tribology Letters, 2004. **17**(3): p. 419-428.

30. Singer, I., *Solid lubrication processes*, in *Fundamentals of Friction: Macroscopic and Microscopic Processes*. 1992, Springer. p. 237-261.
31. Wahl, K.J., R.R. Chromik, and G.Y. Lee, *Quantitative in situ measurement of transfer film thickness by a Newton's rings method.* Wear, 2008. **264**(7): p. 731-736.
32. Wahl, K.J. and I.L. Singer, *Quantification of a lubricant transfer process that enhances the sliding life of a MoS2 coating.* Tribology Letters, 1995. **1**(1): p. 59-66.
33. Shockley, J., S. Descartes, P. Vo, E. Irissou, and R. Chromik, *The influence of Al 2 O 3 particle morphology on the coating formation and dry sliding wear behavior of cold sprayed Al–Al 2 O 3 composites.* Surface and Coatings Technology, 2015. **270**: p. 324-333.
34. Koivuluoto, H. and P. Vuoristo, *Effect of Ceramic Particles on Properties of Cold-Sprayed Ni-20Cr+Al2O3 Coatings.* Journal of Thermal Spray Technology, 2009. **18**(4): p. 555-562.
35. Bowden, F.P. and D. Tabor, *The friction and lubrication of solids*. Vol. 1. 2001: Oxford university press.
36. Zhan, Y. and G. Zhang, *Friction and wear behavior of copper matrix composites reinforced with SiC and graphite particles.* Tribology Letters, 2004. **17**(1): p. 91-98.
37. Deshpande, P. and R. Lin, *Wear resistance of WC particle reinforced copper matrix composites and the effect of porosity.* Materials Science and Engineering: A, 2006. **418**(1): p. 137-145.
38. Shockley, J.M., S. Descartes, E. Irissou, J.-G. Legoux, and R. Chromik, *Third Body Behavior During Dry Sliding of Cold-Sprayed Al-Al2O3 Composites: In Situ Tribometry and Microanalysis.* Tribology Letters, 2014. **54**(2): p. 191-206.
39. Berthier, Y., M. Godet, and M. Brendle, *Velocity accommodation in friction.* Tribology Transactions, 1989. **32**(4): p. 490-496.
40. Berthier, Y., L. Vincent, and M. Godet, *Velocity accommodation in fretting.* Wear, 1988. **125**(1): p. 25-38.
41. Beckmann, N., P.A. Romero, D. Linsler, M. Dienwiebel, U. Stolz, M. Moseler, and P. Gumbsch, *Origins of Folding Instabilities on Polycrystalline Metal Surfaces.* Physical Review Applied, 2014. **2**(6): p. 064004.
42. Rigney, D.A. and S. Karthikeyan, *The evolution of tribomaterial during sliding: a brief introduction.* Tribology Letters, 2010. **39**(1): p. 3-7.
43. Luo, Z.-P., G.-P. Zhang, and R. Schwaiger, *Microstructural vortex formation during cyclic sliding of Cu/Au multilayers.* Scripta Materialia, 2015. **107**: p. 67-70.
44. Yao, B., Z. Han, and K. Lu, *Dry sliding tribological properties and subsurface structure of nanostructured copper at liquid nitrogen temperature.* Wear, 2013. **301**(1): p. 608-614.

Figure captions:

Fig. 1 – Micrographs of as-received Cu (a), MoS_2 (b), and WC (c) powders.

Fig. 2 – Micrographs of cold sprayed Cu-MoS_2 and Cu-MoS_2-WC. (a) cross section of Cu-MoS_2, in which the dark contrast along particle boundaries was identified as MoS_2; (b) an overall view of cross sectional Cu-MoS_2-WC, in which the bright contrast is WC; (c) a top view of the Cu-MoS_2-WC and (d) corresponding EDX map of sulphur distribution. Several dimples in (c) are probably pull-out of particles during sample preparation.

Fig. 3 – Microhardness of Cu-MoS_2 and the matrix of Cu-MoS_2-WC, and pure Cu deposited at the identical condition.

Fig. 4 – Average coefficients of friction (CoFs) of Cu-MoS_2, Cu-MoS_2-WC, and pure Cu in dry nitrogen.

Fig. 5 – Triboimages of Cu-MoS_2 (a) and Cu-MoS_2-WC (b) at 1000 cycles.

Fig. 6 – Wear track topography of Cu-MoS_2 at 100 (a) and 1000 (b) cycles, and Cu-MoS_2-WC at 100 (c) and 1000 (d) cycles.

Fig. 7 – (a) Wear track depth of Cu-MoS_2 and Cu-MoS_2-WC at 100 and 1000 cycles; (b) wear rates of Cu-MoS_2 and Cu-MoS_2-WC at 100 and 1000 cycles.

Fig. 8 – Top view of Cu-MoS_2 wear track at 1000 cycles. (a) Overall features, where detachments are visible, three of them were marked as solid black arrows; (b) and (c) are closer view of the feature indicated in (a), showing detailed morphology of the detachment and cracks, respectively. Cut 1 and cut 2 indicate location of the FIB cuts, the white arrows indicate the direction from which observation were performed. SD marks sliding direction.

Fig. 9 – Optical micrographs of typical features of Cu-MoS_2 wear tracks at 100 (a) and 1000 (c) cycles. (b) and (d) show Raman spectra taken from the spots that are indicated in (a) and (c), respectively. SD indicates sliding direction.

Fig. 10 – Optical micrographs of the counterfaces at 100 (a) and 1000 (b) cycles. (c) Plots of Raman spectra occasionally observed on the debris in contact. SD indicates sliding direction.

Fig. 11 - Top view of Cu-MoS_2-WC wear track at 1000 cycles. (a) Overall features; (b) and (c) closer views of the wear track, showing Cu smeared over WC particles and tongue-shaped structure.

Fig. 12 – (a) Top view of Cu-MoS_2-WC wear track at 100 cycles and (b) corresponding EDX map of sulfur distribution; (c) top view of Cu-MoS_2-WC wear track at 1000 cycles and (d) corresponding EDX map of sulfur distribution. The red dashed lines mark the wear tracks. SD indicates sliding direction.

Fig. 13 - Optical micrographs of the counterfaces at 100 (a) and 1000 (b) cycles. (c) Plots of Raman spectra observed on the debris in contact. SD indicates sliding direction.

Fig. 14 – Subsurface micrographs of Cu-MoS_2 wear track at 100 cycles. (a) Top view of the wear track showing location where the FIB cut was conducted (white line) (Y axis of the image was not corrected). The white arrow indicates direction from which the observation was carried out, the black dashed lines mark the wear track; (b) overall features of the subsurface microstructure; (c) and (d) are detailed microstructure of the location noted in (a) and (b). The red dashed lines indicate interface of the vortices and SD sliding direction.

Fig. 15 – Subsurface micrographs of Cu-MoS_2 wear track at 1000 cycles. (a) Top view of the wear track to show location of the FIB cut; (b) microstructure observation of cut 1, showing detailed sliding-induced microstructure including UFGs, CGs, and MoS_2-containing material; (c) microstructure observation of cut 2, exhibiting various microstructures: vortices of UFGs, CGs, and elongated grains ; (f) a closer view of the area where grain boundaries are not well defined. The red dashed lines are interface of the vortices. SD indicates sliding direction.

Fig. 16 – Subsurface micrographs of the Cu-MoS_2-WC wear track at 100 cycles. (a) (b): microstructure around a WC particle; (c) an EDX map of the area indicated in (a); (d) microstructure that is far from the WC particles. The red dashed lines are interface of the vortices, while the white dashed lines are the interface of sliding-induced and as-sprayed microstructure. SD indicates sliding direction.

Fig. 17 – Subsurface micrographs of the Cu-MoS_2-WC wear track at 1000 cycles. (a) (b) (c): microstructure around a WC particle. (d) microstructure that is far from the WC particles. The red dashed lines are interface of the vortices, while the white dashed lines are the interface of sliding-induced and as-sprayed microstructure. SD indicates sliding direction.

Fig. 1

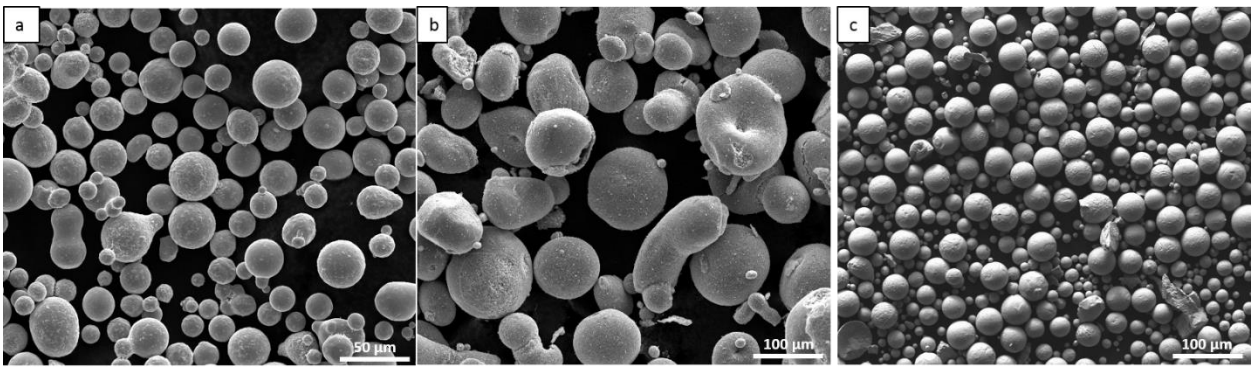

Fig. 2

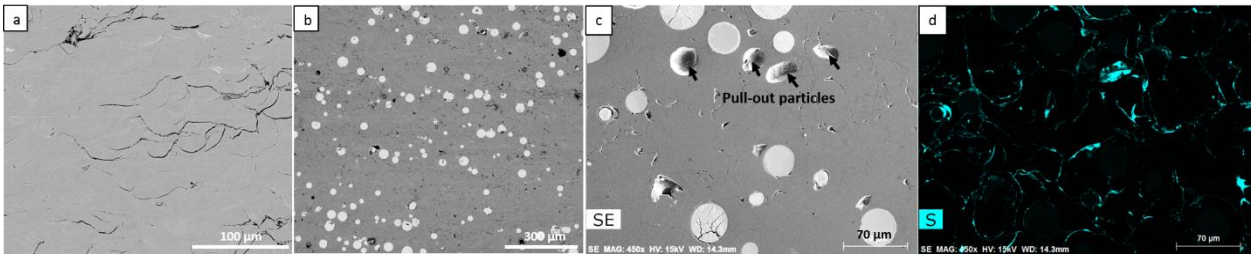
a
b
c
d
Pull-out particles
SE
S
100 µm
300 µm
70 µm

Fig. 3

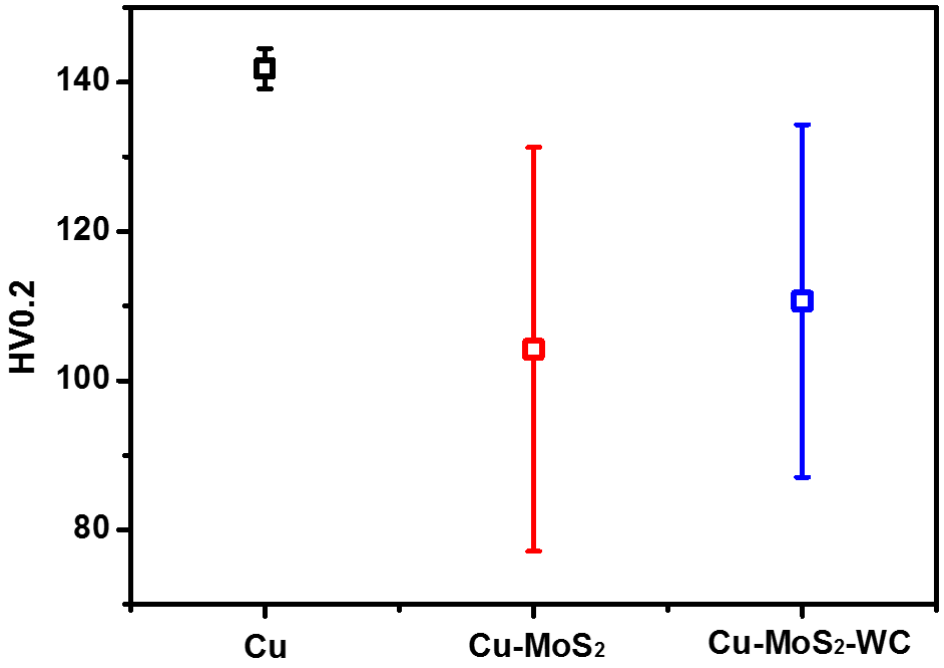
HV0.2
140
120
100
80
Cu
Cu-MoS2
Cu-MoS2-WC

Fig. 4

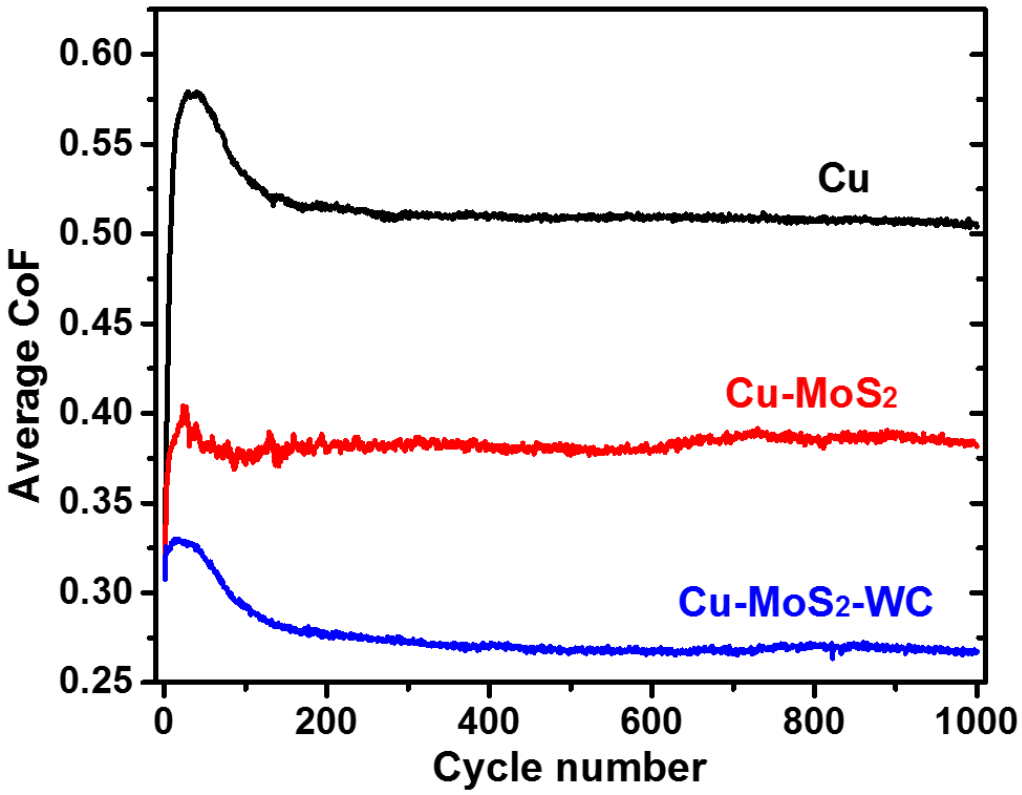
Average CoF
Cycle number
Cu
Cu-MoS2
Cu-MoS2-WC
0.60
0.55
0.50
0.45
0.40
0.35
0.30
0.25
0
200
400
600
800
1000

Fig. 5

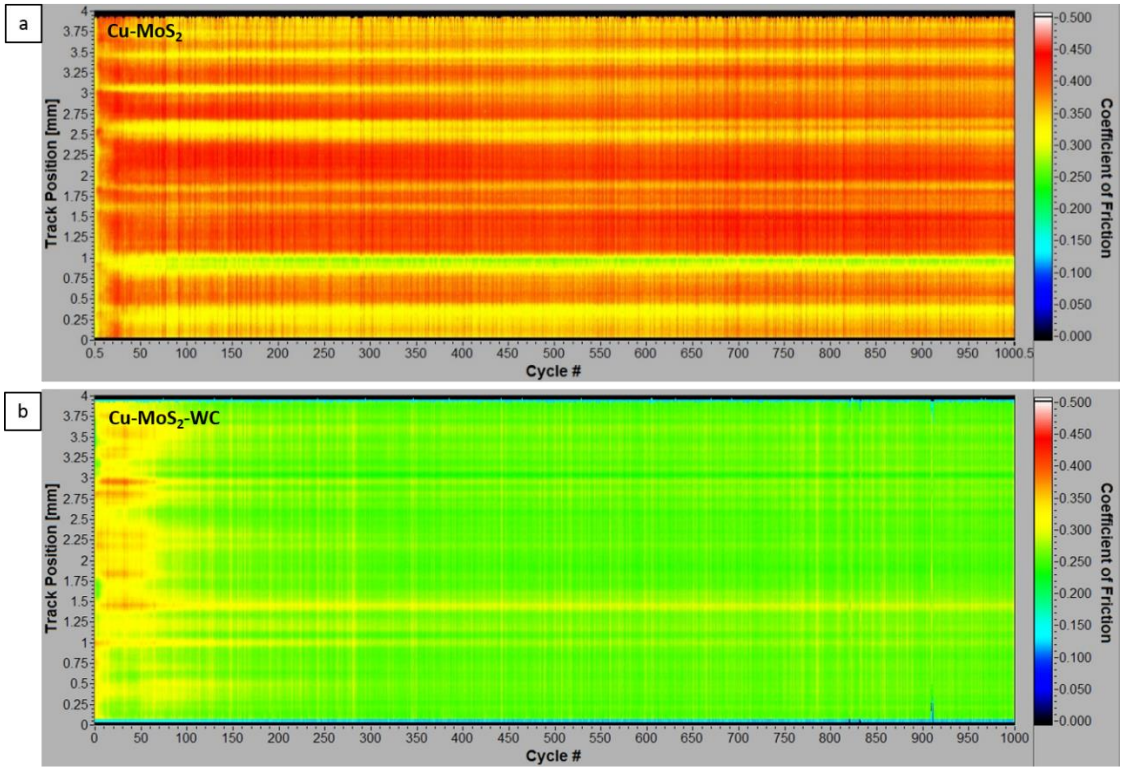
a
Cu-MoS2
Track Position [mm]
Cycle #
Coefficient of Friction
b
Cu-MoS2-WC
Track Position [mm]
Cycle #
Coefficient of Friction

Fig. 6

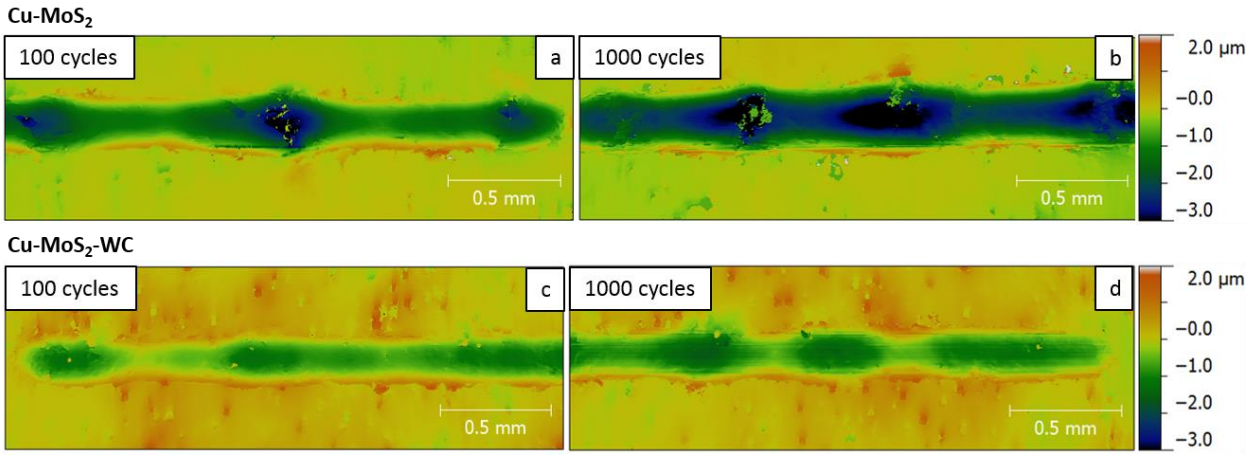

Fig. 7

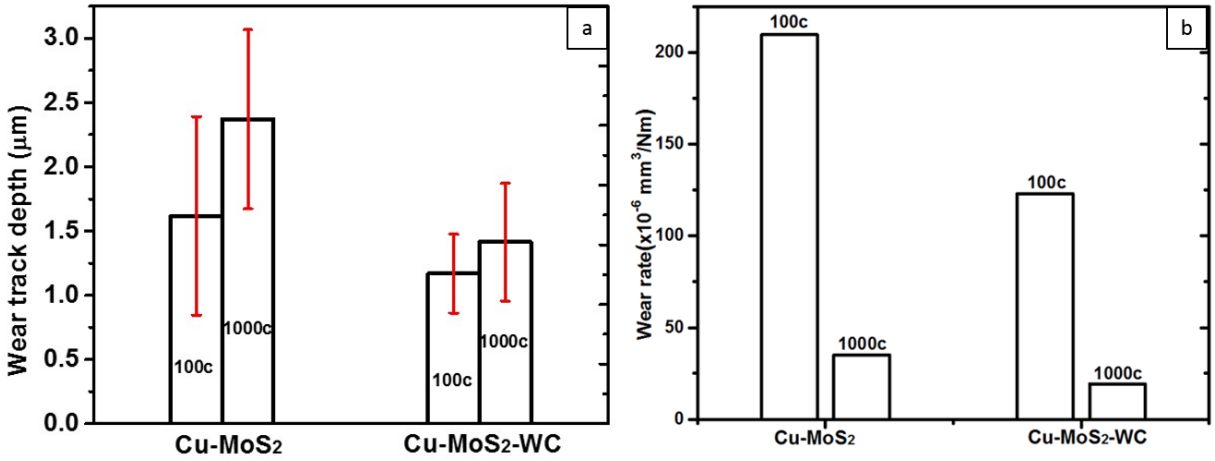

Fig. 8

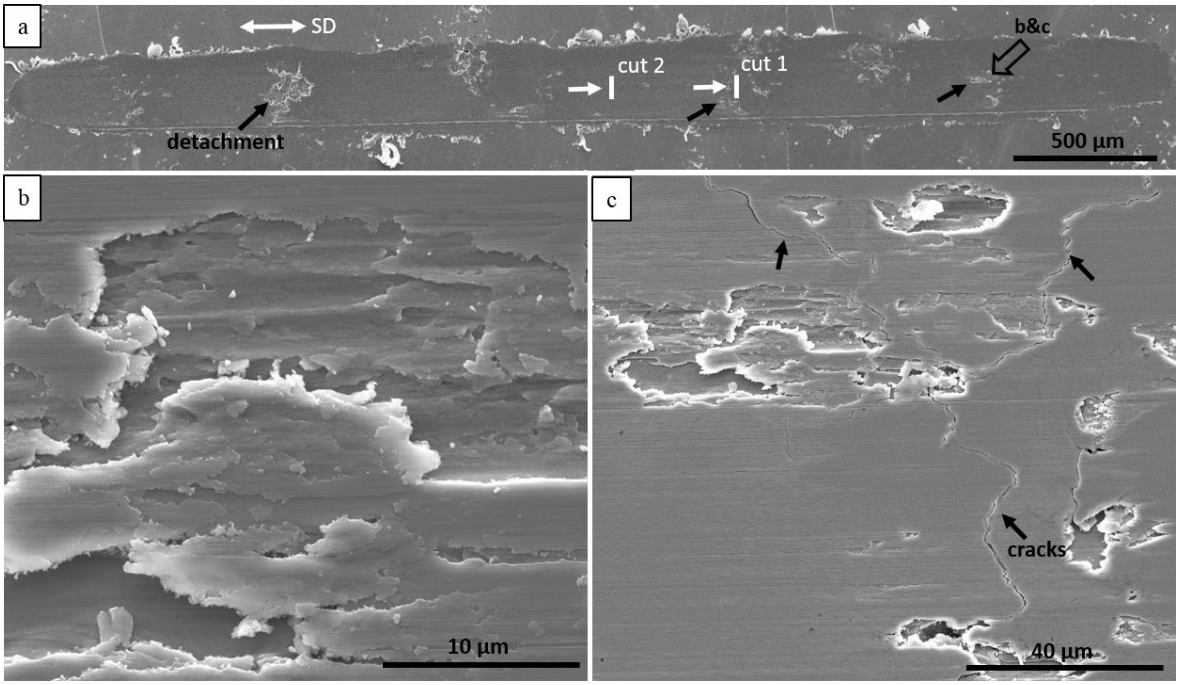

Fig. 9

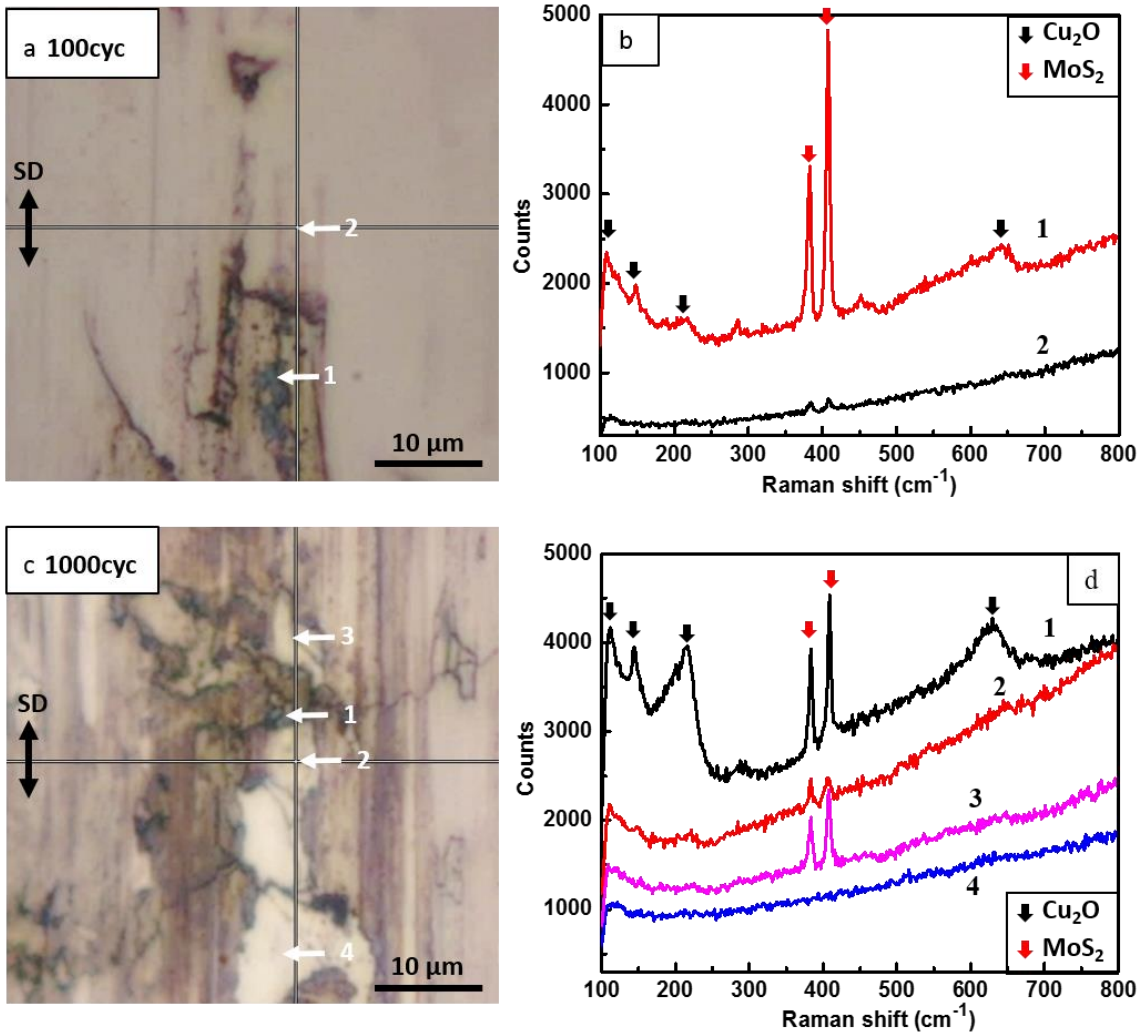
a 100cyc
SD
2
1
10 μm
b
Cu2O
MoS2
Counts
Raman shift (cm-1)
c 1000cyc
3
1
2
4
d

Fig. 10

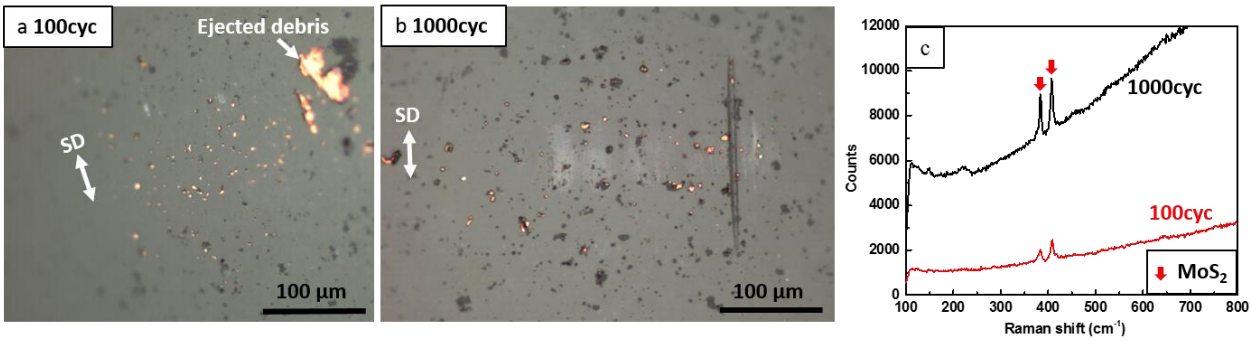
a 100cyc
Ejected debris
SD
100 μm
b 1000cyc
c
1000cyc
100cyc
MoS2
Counts
Raman shift (cm-1)

Fig. 11

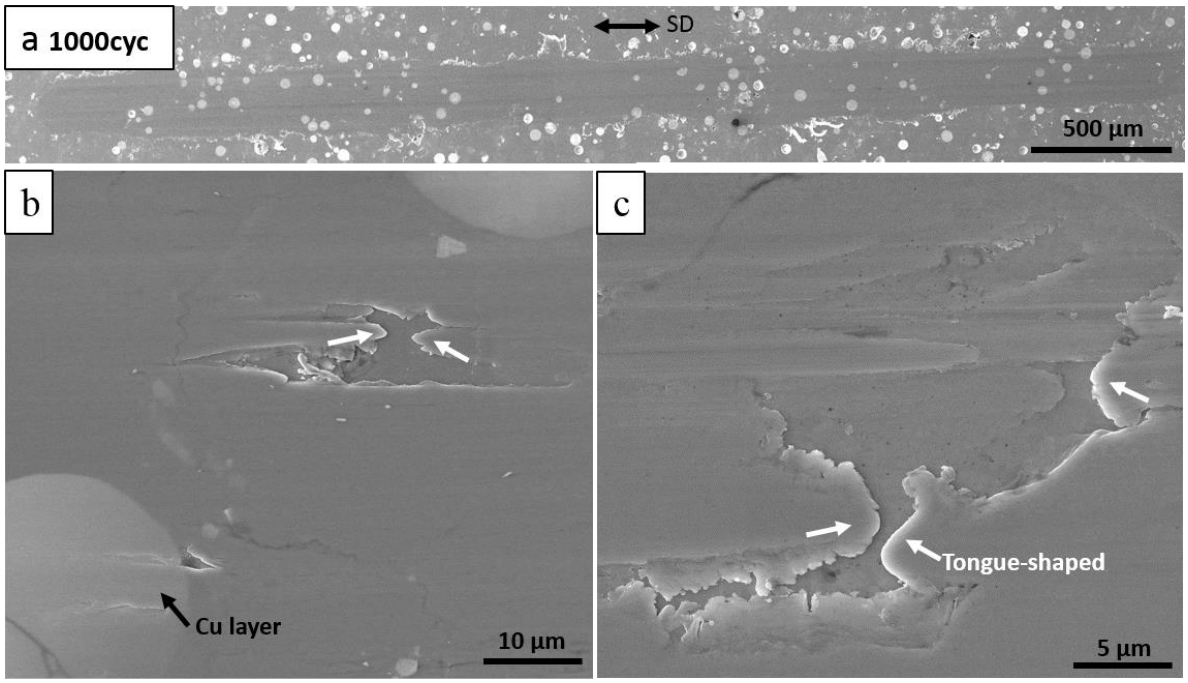
a 1000cyc
SD
500 µm
b
Cu layer
10 µm
c
Tongue-shaped
5 µm

Fig. 12

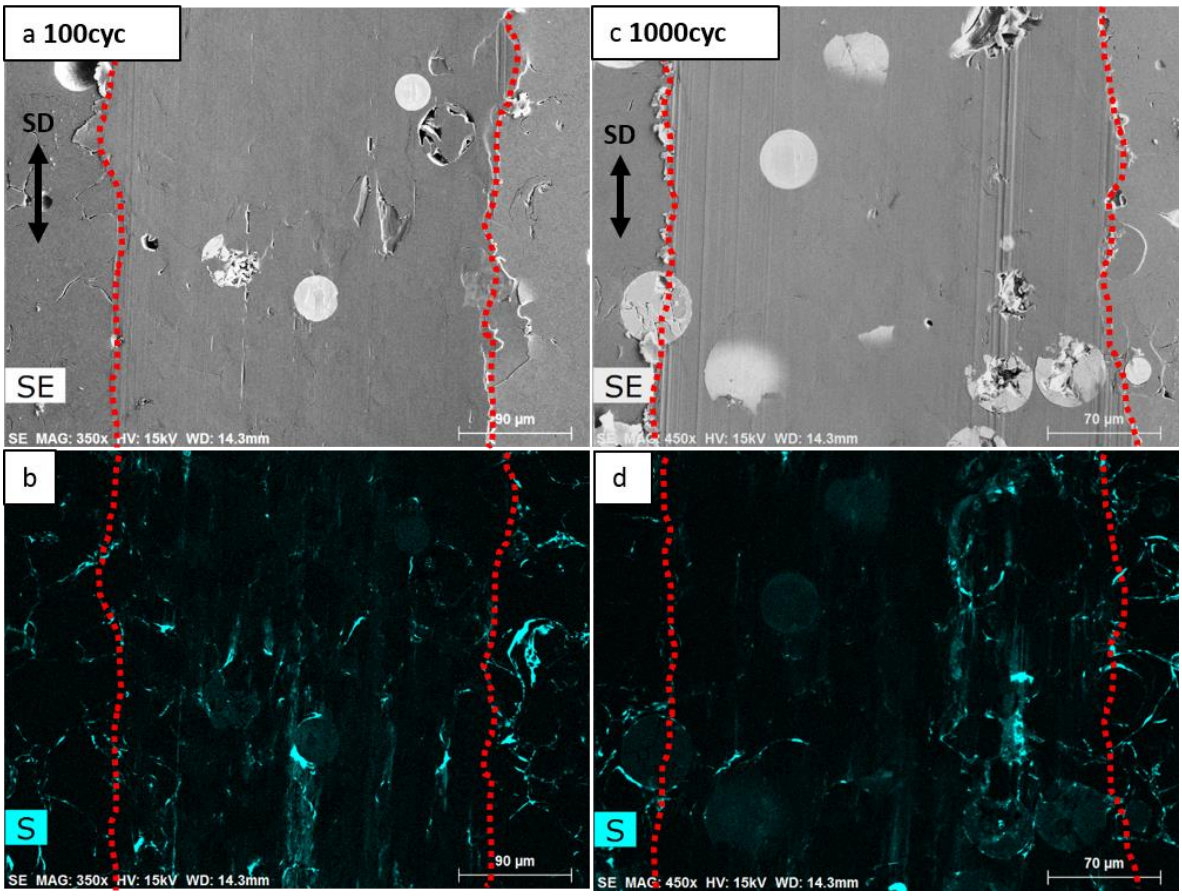
a 100cyc
SD
SE
SE MAG: 350x HV: 15kV WD: 14.3mm
90 µm
c 1000cyc
SD
SE
SE MAG: 450x HV: 15kV WD: 14.3mm
70 µm
b
S
SE MAG: 350x HV: 15kV WD: 14.3mm
90 µm
d
S
SE MAG: 450x HV: 15kV WD: 14.3mm
70 µm

Fig. 13

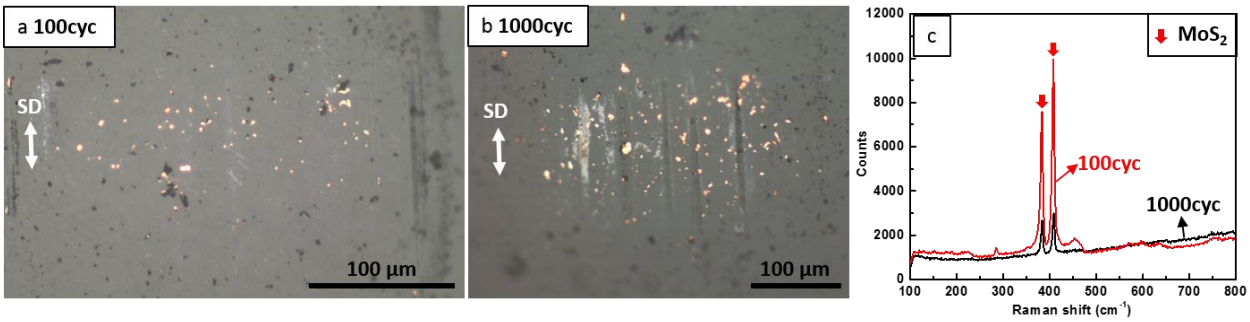

Fig. 14

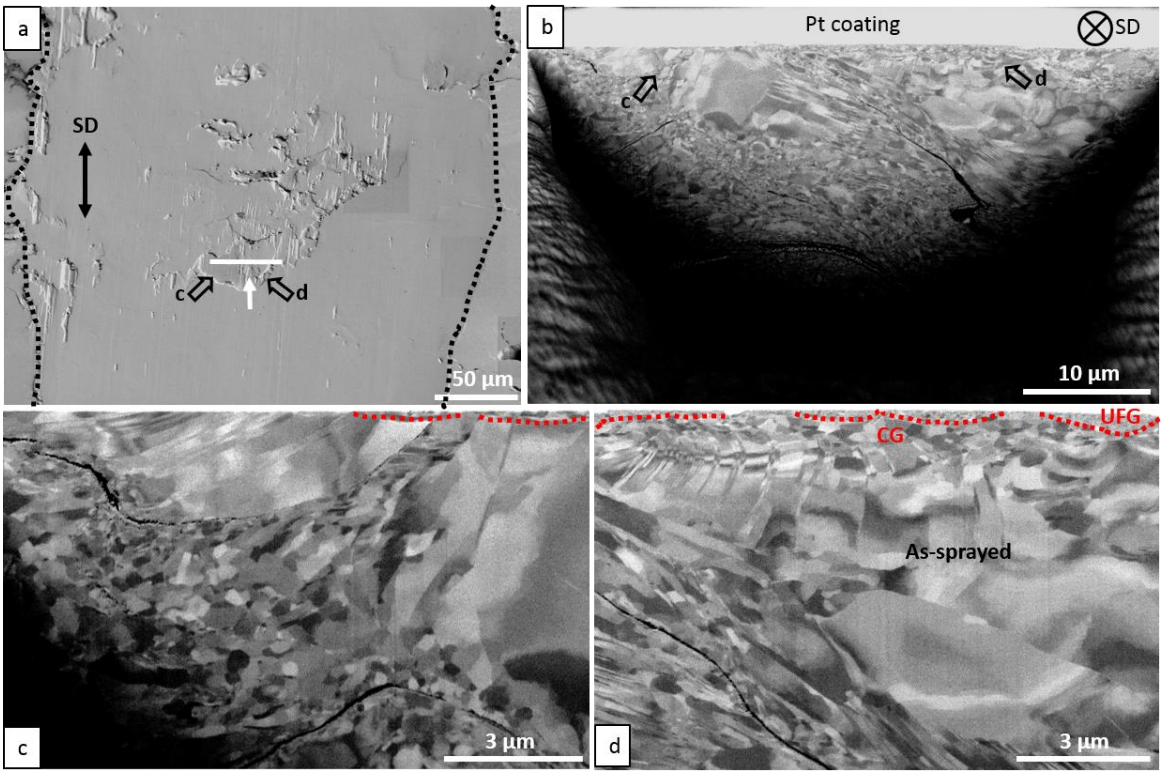

Fig. 15

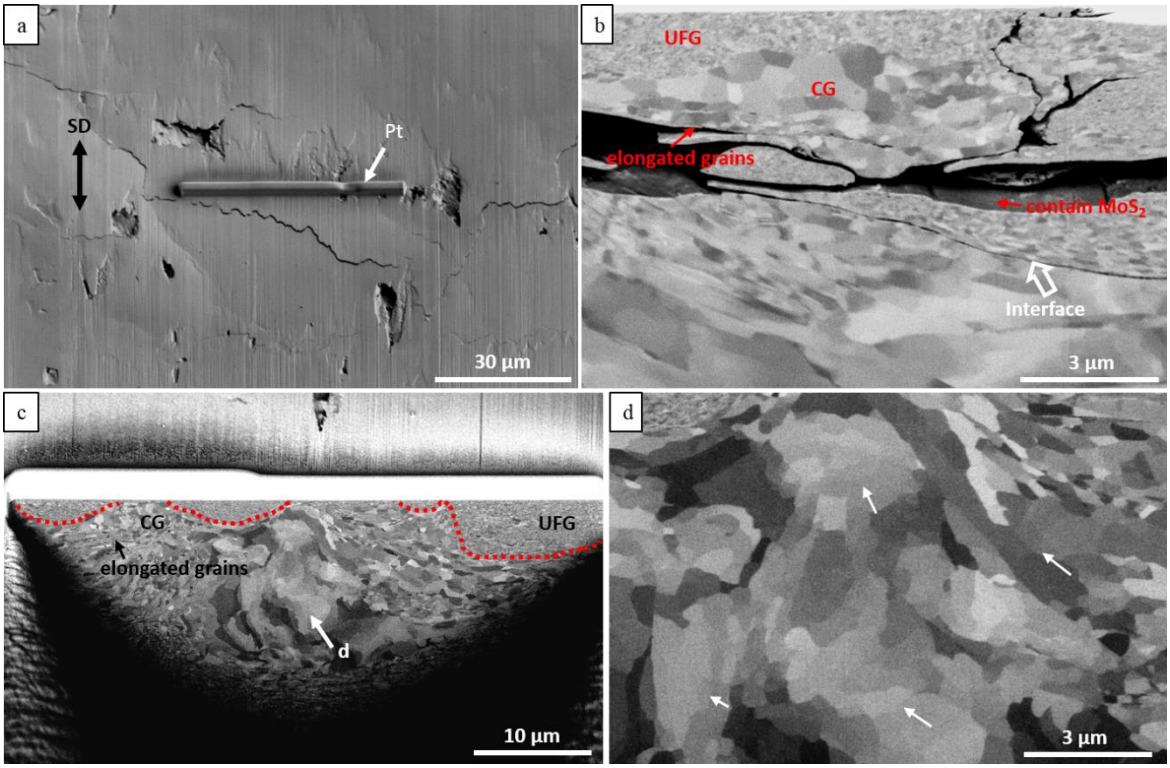
a
SD
Pt
30 μm
b
UFG
CG
elongated grains
contain MoS_2
Interface
3 μm
c
CG
UFG
elongated grains
d
10 μm
d
3 μm

Fig. 16

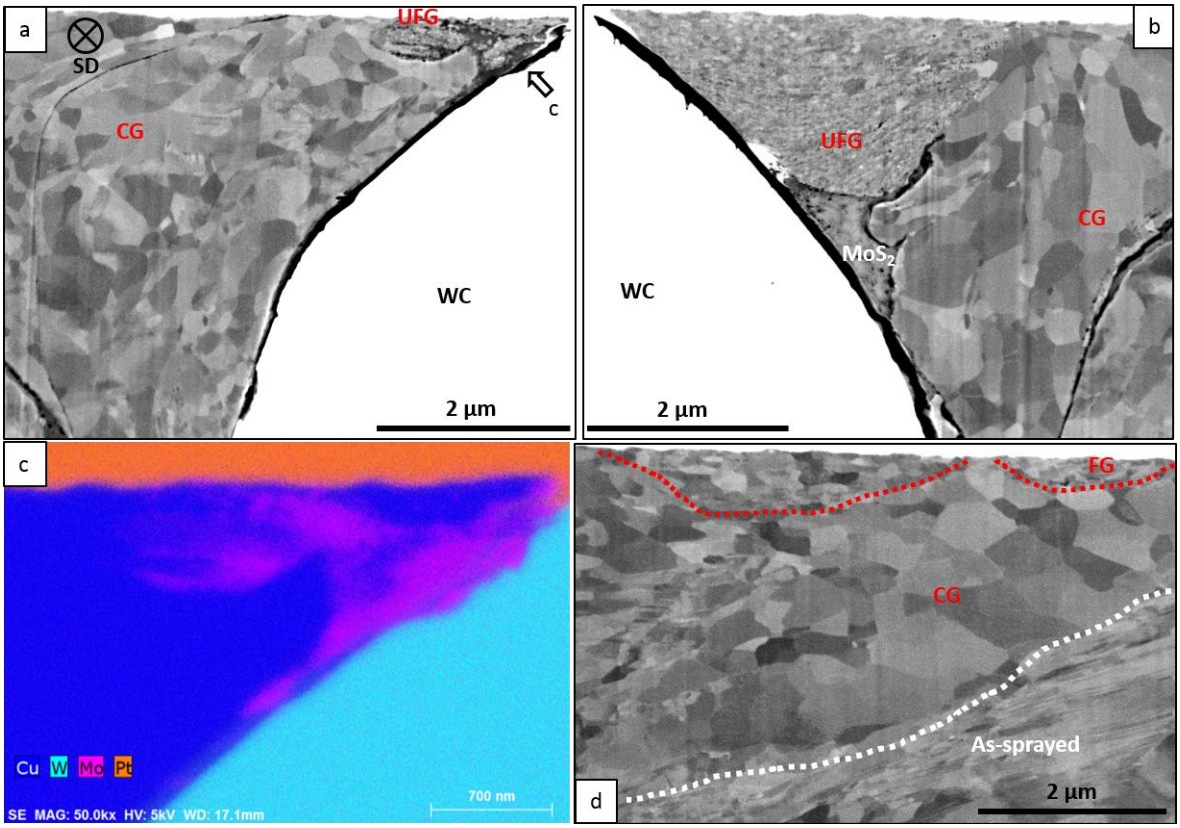
a
SD
UFG
c
CG
WC
2 μm
b
UFG
CG
MoS_2
WC
2 μm
c
Cu W Mo Pt
SE MAG: 50.0kx HV: 5kV WD: 17.1mm
700 nm
d
FG
CG
As-sprayed
2 μm

Fig. 17

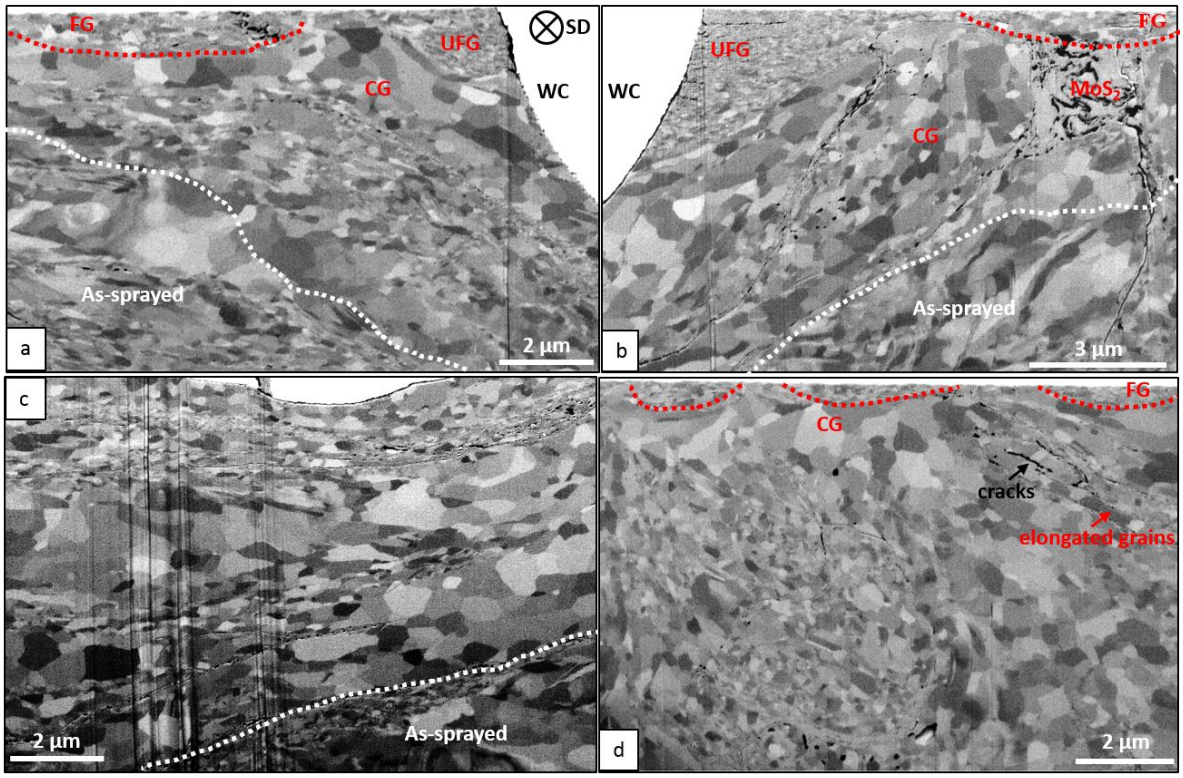
FG
UFG
CG
SD
WC
As-sprayed
a
2 µm
b
UFG
WC
FG
MoS2
CG
As-sprayed
3 µm
c
2 µm
As-sprayed
d
CG
FG
cracks
elongated grains
2 µm